A Novel Nano-Laminated GdB2C2 with Excellent Electromagnetic Wave Absorption Performance and Ultra-High Temperature Thermostability

Longfei Jiang , Gang Qin , Pengxing Cui , Guoqing Wang , Xiaobing Zhou *

Posted Date: 13 May 2024

doi: 10.20944/preprints202405.0725.v1

Keywords: GdB2C2; ternary layered materials; electromagnetic wave absorption; ultra-high temperature ceramic

Article

A Novel Nano-Laminated GdB_2C_2 with Excellent Electromagnetic Wave Absorption Performance and Ultra-High Temperature Thermostability

Longfei Jiang [1,2], Gang Qin [1], Pengxing Cui [2], Guoqing Wang [2] and Xiaobing Zhou [1,2,*]

[1] School of Materials Science and Chemical Engineering, Ningbo University, Ningbo, Zhejiang 315211, China.

[2] Zhejiang Key Laboratory of Data-Driven High-Safety Energy Materials and Applications, Ningbo Key Laboratory of Special Energy Materials and Chemistry, Ningbo Institute of Materials Technology and Engineering, Chinese Academy of Sciences, Ningbo 315201, China.

* Correspondence: zhouxb@nimte.ac.cn (X.B. Zhou)

Abstract: A novel nano-laminated GdB_2C_2 material was successfully synthesized using GdH_2, B_4C, and C *via* an in-situ solid state reaction approach for the first time. The synthesis process of GdB_2C_2 was revealed based on the microstructure and phase evolution investigation. A purity of 96.4 wt. % GdB_2C_2 was obtained at a low temperature of 1500 °C, while a near full pure GdB_2C_2 can be obtained at a temperature over 1700 °C. The as-obtained GdB_2C_2 presented excellent thermal stability at high temperature of 2100 °C in Ar atmosphere due to the stable frame work formed by the high covalent four-members and eight-members B-C rings in GdB_2C_2. The GdB_2C_2 material synthesized at 1500 °C, demonstrates a remarkably low minimum reflection loss (RLmin) of -47.01 dB (3.44 mm) and an impressively broad effective absorption bandwidth (EAB) spanning 1.76 GHz. The possible electromagnetic wave absorption (EMWA) mechanism could be ascribed to the nano-laminated structure and appropriate electrical conductivity, which facilitated to the good impedance matching, remarkable conduction loss, interfacial polarization, along with the reflection and scattering of electromagnetic waves at multiple interfaces. The as-obtained GdB_2C_2, with excellent EMWA performance as well as remarkable ultra-high temperature thermal stability, could potentially serve as an exceptional material for applications in EMWA under conditions of extreme ultra-high temperatures.

Keywords: GdB_2C_2; ternary layered materials; electromagnetic wave absorption; ultra-high temperature ceramic

1. Introduction

Ultra-high temperature ceramics (UHTCs) are materials which usually used at temperatures above 1800 °C. Most UHTCs are highly covalent bonded ceramics, such as transition metal borides and/or carbides[1–3]. Due to the robust covalent linkages established between the transition metal and the boron and/or carbon constituents, the family of UHTCs boasts an array of unparalleled characteristics., including elevated melting points, superior hardness, outstanding mechanical performance at high temperatures, remarkable thermal stability, and commendable resistance to both oxidation and corrosion[4–7]. Therefore, UHTCs are emerging as highly promising candidates for a range of aerospace applications, including the fabrication of nose cone caps and leading edges, and coatings for protection high temperature structure components in hypersonic vehicle, i.e. The protective layers of carbon fiber-reinforced ceramic matrix composites, characterized by their intricate weave of carbon filaments embedded within a resilient ceramic framework, offer a synergistic blend of strength and durability[8,9].

On the other hand, for the aerospace applications, the UHTCs not only should have high temperature thermal stability, but also possess desirable functional capability, such as excellent electromagnetic wave absorption (EMWA) performance[10–12]. Numerous EMWA materials have been investigated, such as carbon-based materials[13–16], magnetic metal materials[17,18], ferrite as

 doi:10.20944/preprints202405.0725.v1

well as their composites[19], and polymer matrix composites[20]. Magnetic materials, such as ferrite exhibit excellent EMWA performance, but it lacks dielectric loss capacity, once they exceed the Curie temperature, their magnetic properties disappear, rendering the magnetic loss mechanism ineffective[19]. Polymer-based composites which are lightweight and high design flexibility. However, the materials in question possess a relatively low melting point, rendering them ill-suited for high-temperature applications where elevated thermal resistance is a critical requirement[20,21]. In addition, there are carbon-related materials such as carbon fiber, carbon nanotubes, and graphene that exhibit characteristics of reduced weight, lower density, enhanced electrical conductivity, and superior mechanical properties[14–16,22–29]. However, they typically exhibit a high dielectric constant and low permeability, resulting in suboptimal impedance matching and hindered electromagnetic wave penetration into the material. Additionally, their susceptibility to oxidation in high temperature environments renders them unsuitable for applications at elevated temperatures[30]. The task of achieving a material with a relatively broad effective absorption bandwidth and enhanced electromagnetic wave absorption performance poses a formidable challenge. Additionally, these materials must exhibit low density, thin thickness, and exceptional thermal stability even under extreme temperatures, such as stealth materials of high-speed military vehicles[31].

Rare earth diborocarbides (REB_2C_2, RE=Sc, Y, and lanthanide elements) are a group of laminated structure materials like MAX phase (M represents a transition metal, A denotes elements from groups IIIA, IVA, VA or VIA, and X stands for carbon or nitrogen)[32–35]. For GdB_2C_2 (RE is Gadolinium, Gd), it belongs tetragonal structure with space group of P4/mbm (No.127)[36]. Gd atoms arranged in alternating B-C layers along the z-axis direction. Gd-Gd bonds are metallic bonds, while B-C bonds are covalent bonds, which form four-members and eight-members B-C rings. These anisotropy structure of chemical bonds resulting in the GdB_2C_2 may shows strong anisotropy in physical properties[37,38]. Such as the magnetic properties of GdB_2C_2, it was demonstrated that it shown antiferromagnetic in the c plane, while it was ferromagnetic along the c axis[39]. The resistivities of GdB_2C_2 were reported decreased with decreasing temperature, which shown a metallic conductivity and elcctron-type conductors[40].

On the other hand, most of the reported synthesis method on REB_2C_2 were YB_2C_2[41,42]. There are few studies on the fabrication method of GdB_2C_2[40]. The single-crystal GdB_2C_2 was synthesized using Gd, B, and C as raw materials via arc-melted process for several times. The samples were subsequently sealed in an evacuated silica tube for several days[36]. The other represent synthesis procedure of GdB_2C_2 was two-step procedure, including the GdB_4 fabricated by induction heating mixtures of Gd and B at 1900 °C. Then the GdB_4 and graphite heated at 1900 °C for three hours to get GdB_2C_2 [40]. In addition, to the best of the authors knowledges, there is few reports on the one-step synthesis method of GdB_2C_2 powders and its electromagnetic wave performance as well as the thermal stability at ultra-high temperatures. Considering the typical nano-laminated structure of GdB_2C_2, it may show excellent electromagnetic wave absorption performance owing to the potential multiple interfaces scattering loss as well as the dielectric loss mechanisms exist in the GdB_2C_2 like MAX phases[32,33,43–46].

Consequently, the principal objective of this research endeavor is to pioneer a straightforward, single-step manufacturing process for the creation of the nano-laminated GdB2C2 material, while simultaneously elucidating the intricate electromagnetic wave absorption mechanism at play. In addition, the thermal stability at an ultra-high temperature of 2100 °C was investigated for the potential aerospace applications of GdB_2C_2.

2. Experimental Procedure

2.1. Materials

In the pursuit of synthesizing GdB_2C_2, the foundational elements of GdH_2, B_4C, and carbon black were employed as the raw materials. The GdH_2 powders, boasting a purity exceeding 99.9% and an average grain dimension of approximately 70 micrometers, were sourced from the esteemed Hunan

 doi:10.20944/preprints202405.0725.v1

Rare Earth Metal Materials Research Institute Co., Ltd., situated in the vibrant city of Changsha, China. The B_4C powders, with a purity surpassing 99% and a typical particle size of around 500 nanometers, were procured from the innovative Suzhou Nutpool Materials Technology Co., Ltd., nestled in the city of Jian, China. Complementing these, the carbon black powders, characterized by a purity of 99.9% and a similar mean particle size of 500 nanometers, were acquired from the proficient EnoMaterial Co., Ltd., located in the industrious city of Qinhuangdao, China.

2.2. Fabrication of GdB_2C_2

The GdH_2, B_4C and Carbon black powders were mixed in a glovebox under an argon atmosphere with a molar ratio of GdH_2:B_4C:C = 2:1:3. To investigate the in-situ reaction process of GdB_2C_2, the mixed powders were fired at various temperatures ranging from 900 °C to 1800 °C for 4 h in a graphite furnace under an argon atmosphere. The powder undergoes heating and cooling at a rate of 5 °C/min, followed by grinding in an agate mortar for a duration of 40 minutes. Figure 1 shows the schematics of the GdB_2C_2 powder synthesis procedures.

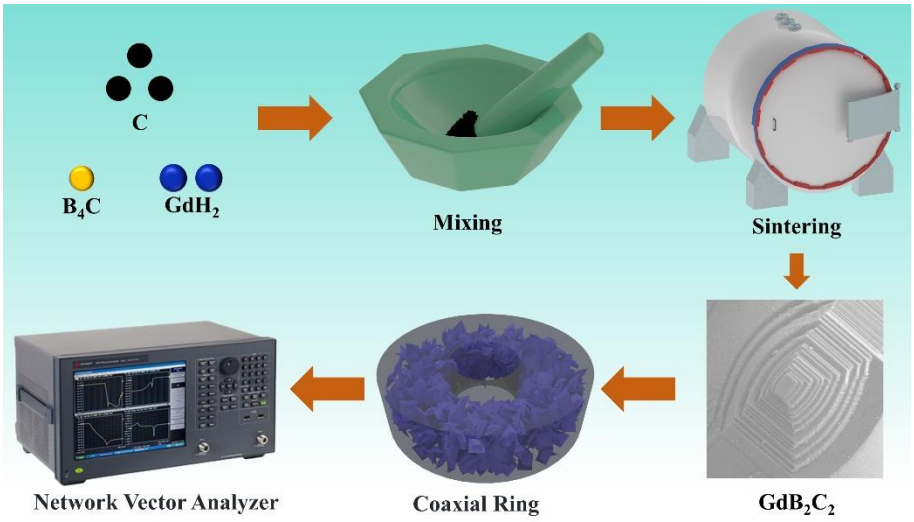

Figure 1. Schematic of GdB_2C_2 powder synthesis procedures and EMWA property test.

2.3. Characterizations

The composition of phases and crystalline structures within the samples synthesized at different temperatures were scrupulously evaluated using a Bruker AXS D8 Advance X-ray diffractometer, procured from Germany, which operates on Cu Kα radiation with a wavelength set at λ = 1.5406 Å. The power parameters for this instrument were set at 1600 W, equating to a current of 40 mA and a voltage of 40 kV, while utilizing a step scan methodology of 0.02°/2θ with a step duration of 0.2 seconds. The constituents of the phases and parameters of the lattice within the resulting materials were deciphered through the Rietveld refinement processing of the XRD patterns, facilitated by the TOPAS-Academic v6 software suite. The microscopic attributes of the specimens, synthesized under a range of temperature environments, were meticulously examined leveraging a scanning electron microscope (SEM; model Regulus 8230, produced by Hitachi, Japan), complemented with an energy-dispersive spectroscopy (EDS) system. The average grain dimensions were quantified by analyzing a selection of SEM micrographs, with a rigorous count of no less than 100 grains per sample. To corroborate the microstructural and phase attributes of the GdB_2C_2 synthesized at 1500 °C, transmission electron microscopy (TEM; model Talos F200x by Thermo Fisher Scientific, USA) was engaged, we conducted an in-depth analysis of the samples. The specimens were prepared for TEM observation using a focused ion beam (FIB) apparatus provided by Aurgia, associated with Carl Zeiss, USA, which facilitated the production of the requisite thin foils.

The influence of temperatures applied during heat treatment on the electromagnetic wave absorption (EMWA) capabilities of the samples was examined. This was done by measuring their

 doi:10.20944/preprints202405.0725.v1

complex permittivity and permeability at high temperatures of 1500 and 1800 °C over a 2 to 18 GHz frequency band, using a Keysight E5063A Network Analyzer. For these measurements, we fabricated a toroidal ring using GdB_2C_2 powder mixed with paraffin in a 60-volume percent ratio. The ring's dimensions were set to thickness of 2 mm, inner diameter of 3 mm and outer diameter of 7 mm.

3. Results and Discussion

3.1. Microstructure and Phase Composition of GdB_2C_2

Figure 2a,b present the X-ray diffraction (XRD) profiles of the powders immediately post-synthesis, encompassing a temperature spectrum from 900 to 1800 °C. GdB_4, Gd-C and Gd_2O_3 phase was detected at the temperature of 900 °C, besides the residual un-reacted raw materials of GdH_2, B_4C and C. As the synthesis temperature increased to 1100-1300 °C, GdB_2C_2 was formed, while GdB_4 and Gd-C phase was still detected, which implied that the reaction was not completed. When the temperature increased to 1400-1500 °C, GdB_2C_2 was the main phase, just a small amount of GdB_4 impurity phase was detected. While the temperature increased to 1600-1800 °C, a near full pure GdB_2C_2 was obtained.

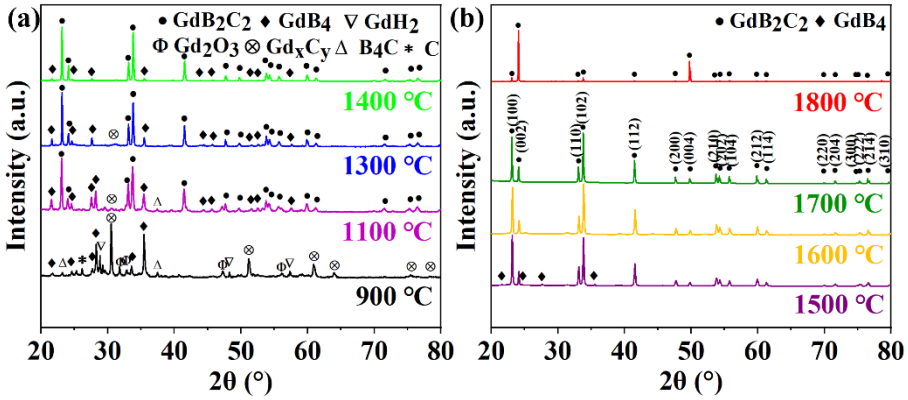

Figure 2. XRD patterns of GdB_2C_2 fabricated at different temperatures (a) 900 °C-1400 °C (b) 1500 °C-1800 °C.

The Rietveld refinement analysis revealed a progressive enrichment of the GdB_2C_2 phase, escalating from 95.47 wt. % to a pure 100 wt. % as the synthesis temperature was elevated from 1400 to 1700 °C. Concurrently, the presence of the GdB_4 impurity diminished, reducing from 4.53 wt.% to an undetectable level. Figure 3 shows a representative the XRD pattern (Rietveld refinement) for GdB_2C_2 synthesized at 1500 °C, the resultant reliability factors (R_{wp} = 9.4 %) affirm the crystallization of GdB_2C_2 in a tetragonal configuration, as depicted in the inset of Figure 3. The lattice parameters a and c were determined to be approximately 3.78 Å and 7.27 Å, respectively, the data presented in Table 1 demonstrates the close conformity of this component to the reported lattice parameters of GdB_2C_2[40]. The lattice parameter findings were corroborated by the complementary TEM analysis, which substantiated the value of c at 7.5612 Å through selected area electron diffraction (SAED) and high-resolution transmission electron microscopy (HR-TEM) imaging of the GdB_2C_2 powders. These observations are presented in Figure 4a,b. The HR-TEM image elucidates the atomic arrangement along the zone axis, revealing a lattice fringe spacing of 0.37806 nm, which corresponds to the (002) crystal plane of GdB_2C_2. The experimentally determined spacing of the (002) plane, as depicted in Figure 4b, closely approximates the theoretical value for GdB_2C_2, thereby substantiating the successful synthesis of the GdB_2C_2.

Table 1. The Rwp, lattice parameters (*a* and *c*) and amounts of GdB_2C_2 and GdB_4 phase in the as-obtained powders fabricated at various temperatures according to Rietveld refinement results.

Holding	Rwp	Experimental	GdB_2C_2	GdB_4

 doi:10.20944/preprints202405.0725.v1

temperature (°C)		a (Å)	c (Å)	(wt%)	(wt%)
1400	8.4	3.78	7.28	95.47	4.53
1500	9.4	3.78	7.27	96.38	3.62
1600	8.4	3.79	7.27	99.24	0.76
1700	8.3	3.79	7.27	100	0

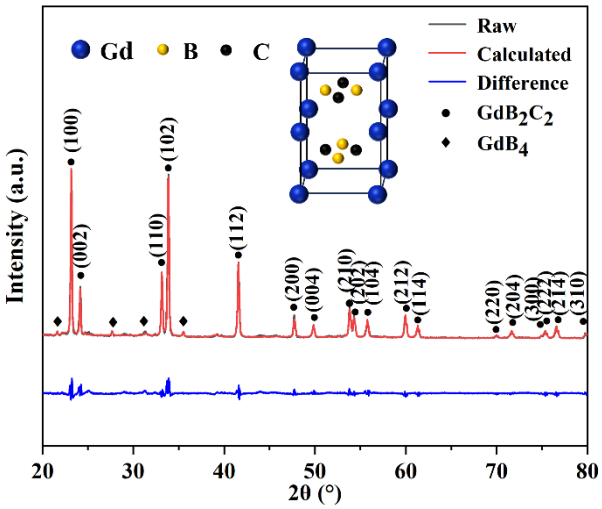

Figure 3. Rietveld refinement of XRD pattern of GdB_2C_2 synthesized at 1500°C.

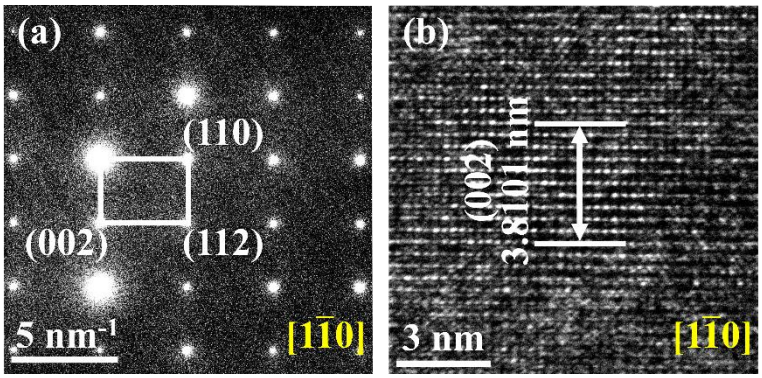

Figure 4. (a) SAED pattern (b) HR-TEM image of GdB_2C_2 synthesized at 1500 °C.

According to the phase evolution analysis of the samples fabricated at various temperatures, the formation process of GdB_2C_2 *via* the in-situ reaction among the GdH_2, B_4C, and C could be concluded as follow. At the low temperature of 900 °C, GdH_2 did dehydrogenation and decomposed to Gd and H_2 (reaction 1)[47]. The generated Gd diffused on the surface of B_4C and C and reacted with them to form GdB_4 and Gd-C phase (reaction 2). At the temperature ranging of 1100-1300 °C, the intermediate phase of GdB_4 and Gd-C further reacted with the residual C, the GdB_2C_2 was beginning formed (reaction 3). While the grain size was only several hundred nanometers due to the low synthesis temperature (Figure 5a). As the temperature increased to 1400 °C, most of the GdB_4 and Gd-C intermediate phases were transformed to GdB_2C_2. Most of the GdB_2C_2 particles were in size of 0.5-1 μm, while there were still some nano-sized particles were observed (Figures 5b and 6a). When the temperature increased to 1500 °C, the GdB_2C_2 grains growth along with the nano-sized particles disappeared (Figure 5c). The mean particle size was around 1.1 μm (Figure 6b). As the temperature increased to over 1600 °C, almost pure GdB_2C_2 was obtained. At these high temperatures range, the

 doi:10.20944/preprints202405.0725.v1

GdB_2C_2 grains growth rapidly. The mean particle size can be increased from 4.76 μm to 16.44 μm as the temperature increased from 1600 to 1800 °C (Figure 6c–e). The typical layered structure of GdB_2C_2 was observed (Figure 5d–f). Noted that the GdB_2C_2 grains were preferred growth along the *c* plane, as a result the (002) diffraction peak was emphasized as the highest peak for the sample fabricated at 1800 °C (Figure 2b). This phenomenon was also observed in the single crystal GdB_2C_2[38].

$$GdH_2 \rightarrow Gd + H_2 \quad (1)$$

$$2Gd + B_4C + C \rightarrow GdB_4 + GdC_2 \quad (2)$$

$$GdC_2 + GdB_4 + 2C \rightarrow 2GdB_2C_2 \quad (3)$$

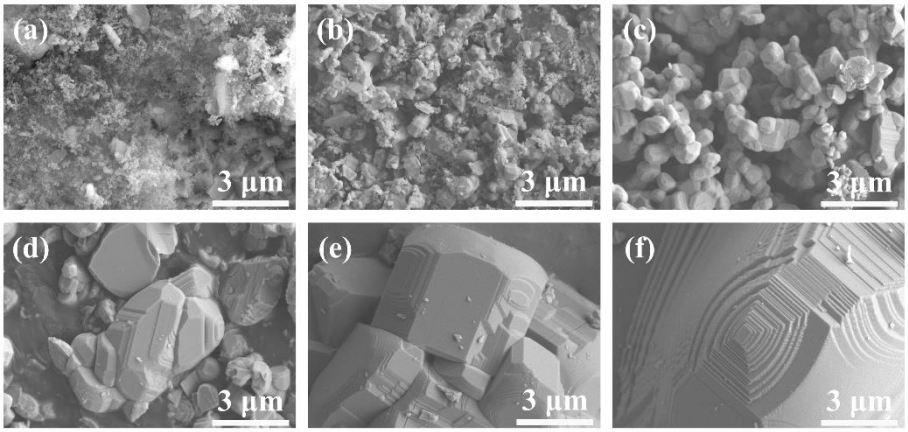

Figure 5. SEM images of GdB_2C_2 powders fabricated at varying temperatures (a) 1300 °C, (b) 1400 °C, (c) 1500 °C, (d) 1600 °C, (e) 1700 °C, and (f) 1800 °C.

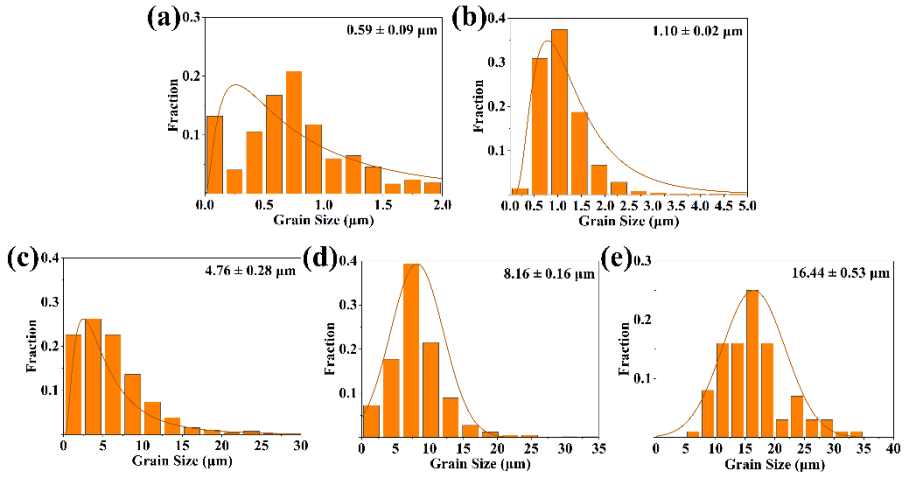

Figure 6. Particle size distribution of GdB_2C_2 powders fabricated at varying temperatures obtained by SEM images analysis (a) 1400 °C, (b) 1500 °C, (c) 1600 °C, (d) 1700 °C and (e) 1800 °C.

3.2. Ultra-High Temperature Thermal Stability of GdB_2C_2 at 2100 °C

Thermal stability at high temperature is a critical property for the applications of UHTCs. Figure 7a–c shows the morphology of GdB_2C_2 powders (prepared at 1500 °C) after heat treatment at 2100 °C for 20 minutes under argon atmosphere. The obvious grain growth was observed. The maximum length of the GdB_2C_2 can be around 30 μm, which was significantly increased up to 30 times larger than that of the original as-synthesized GdB_2C_2 sample (~1.1 μm). The fracture surface SEM image (Figure 7c) shows a typical nano-laminated structure similar MAX phases. The laminated fracture,

 doi:10.20944/preprints202405.0725.v1

such as delamination, slipping, and kink band was observed (Figure 7c), which suggests the ductile nature of the GdB_2C_2.

The phase composition of the heat-treated GdB_2C_2 sample is depicted in Figures 7d,e. Upon heat treatment at 2100 °C, no significant phase transition was observed in GdB_2C_2. However, careful examination of the post-heat treatment phase reveals an enhancement in the diffraction peaks intensity for (002) and (004) crystallographic planes. Additionally, the characteristic diffraction peaks of the (100) and (002) planes for the heat-treated sample at 2100 °C exhibit a shift towards higher 2 theta angles when contrasted with the as-obtained GdB_2C_2 powders. This shift implies a contraction in the lattice parameters of the GdB_2C_2 following the heat treatment at 2100 °C, relative to the as-obtained state.

After undergoing heat treatment, it was observed that the lattice parameters exhibited a decrease, which can be attributed to the volatilization of Gd atoms. Subsequent volatilization of Gd atoms led to the formation of vacancies within the crystal structure, consequently resulting in a reduction in lattice parameters, This interpretation is corroborated by the crystalline framework of GdB_2C_2, which comprises Gd-B and Gd-C bonds with lengths of 276.4 and 272.0 pm, respectively, complemented by shorter B-C bonds (162.2 pm and/or 151.2 pm)[36]. The bond energies of the Gd-B and Gd-C interactions are notably lower than those of the B-C bonds, rendering the former more susceptible to dissociation at the elevated temperatures of 2100 °C. Consequently, Gd atoms preferentially evaporate from the surface of the material. The evaporation of Gd atoms and the consequent vacancies would naturally result in a contraction of the lattice, as the remaining atoms reposition to maintain the integrity of the crystal structure. In contrast, the highly covalent four-membered and eight-membered B-C rings remain intact and do not undergo evaporation. This observation underscores the pivotal role of these B-C rings in conferring ultra-high temperature thermal stability to GdB_2C_2. A comparable behavior has been noted in the analogous YB_2C_2 materials, further supporting the significance of these covalent B-C ring structures in maintaining the thermal stability of related compounds[42].

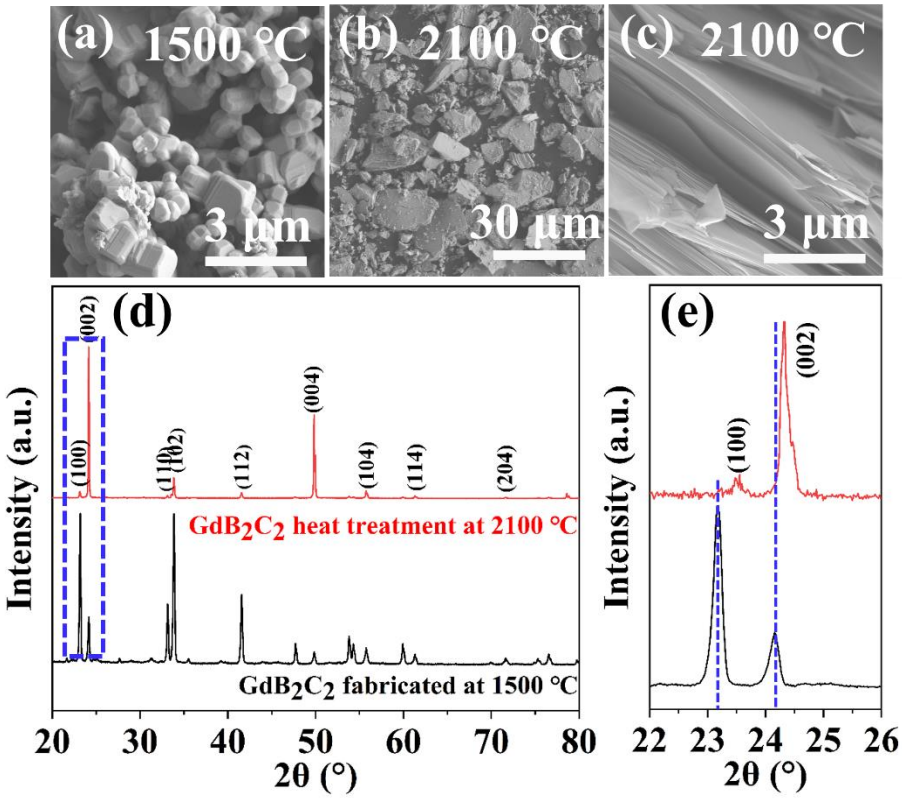

 doi:10.20944/preprints202405.0725.v1

Figure 7. SEM images of GdB_2C_2 powders at (a) 1500°C and heat treatment at (b)(c) 2100 °C, (d) XRD pattern of the as-synthesized GdB_2C_2 at 1500°C and the sample after heat treatment at 2100 °C (e) partial XRD patterns showing a peak shift of (002).

3.3. Electromagnetic Wave Absorption Properties of GdB_2C_2

The performance of a material in interacting with electromagnetic waves is influenced by multiple factors. The effectiveness of impedance matching dictates the ability of the electromagnetic wave to permeate and be absorbed by the material; poor impedance matching leads to the wave's direct reflection. The complex dielectric constant and complex permeability reflect the material's aptitude for absorbing electromagnetic waves, which in turn determines its efficiency in transforming them into alternative forms of energy[48].

To investigate the effect of synthesis temperature on the electromagnetic wave absorption (EMWA) characteristics of GdB_2C_2 powders, an assessment was conducted on powders prepared at 1500 °C and 1800 °C. This evaluation included the measurement of their complex permittivity and permeability. The real and imaginary parts of the complex permeability for both temperatures were found to be approximately 1 and 0, respectively, across the frequency range of 2 to 18 GHz. This indicates that the magnetic loss in these materials is negligible and thus not a factor in their EMWA characteristics. Consequently, the EMWA properties of the GdB_2C_2 powders are predominantly governed by the complex permittivity [49,50].

The two components of the powder synthesized at 1500 °C and 1800 °C are depicted in Figure 8, representing the real (ε′) and imaginary (ε″) parts of the complex permittivity. These components can be expressed using Debye's theory as follows This theoretical approach provides a means to interpret and analyze the dielectric behavior of the materials under investigation[51]:

$$\varepsilon' = \varepsilon_\infty + (\varepsilon_s - \varepsilon_\infty)/\left(1+(\omega\tau)^2\right) \quad (4)$$

$$\varepsilon'' = (\varepsilon_s - \varepsilon_\infty)/\left(1+(\omega\tau)^2\right) + \delta_{ac}/\omega\varepsilon_0 = \varepsilon_p'' + \varepsilon_c'' \quad (5)$$

Within the context of Debye theory, the dielectric constants ε_0, ε_s, and ε_∞ are respectively indicative of the permittivity in free space, at a static state, and at the frequency of light. The variable ω denotes angular frequency, τ signifies the polarization relaxation tim, while ε_p'' and ε_c'' indicate the roles of polarization loss and conductance loss in the imaginary component of the dielectric constant, respectively. Conventionally, ε′ is indicative of the dielectric material's capacity for energy storage, whereas ε″ reflects the dissipation of dielectric energy.[52,53]. Furthermore, the dielectric loss tangent, denoted as $\tan\delta_e$ and calculated as the ratio of ε′ to ε″, is commonly employed to evaluate the dielectric attenuation of the sample. This parameter, as depicted in Figure 8c, it is an indicator of the attenuation ability of electromagnetic wave absorbing material to electromagnetic wave. The dielectric loss tangent provides a quantitative measure of the efficiency with which the material can attenuate incident EMWs.

 doi:10.20944/preprints202405.0725.v1

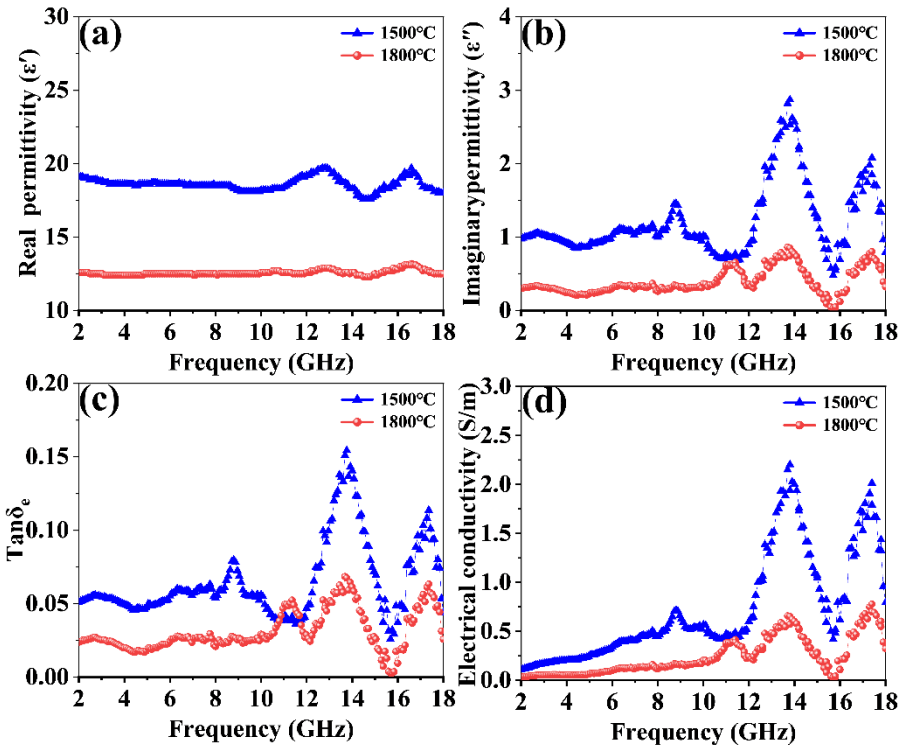

Figure 8. Real (a) and imaginary (b) parts of the complex permittivity, dielectric loss angle (c) and electrical conductivity (d) of the GdB_2C_2 synthesized at 1500 °C and 1800 °C.

Both of the ε′ and ε″ of the GdB_2C_2 powders synthesized at 1500 °C were higher than those of the samples synthesized at 1800 °C, confirming that the fine particle size could promote the dielectric properties of GdB_2C_2. The finer grain size, the more interfaces were formed between GdB_2C_2 powders and paraffin matrix. The improvement of interaction between the GdB_2C_2-paraffin and the enhancement of interfacial polarization contribute to the higher ε′ of GdB_2C_2 powders synthesize at 1500 °C compared to the sample synthesized at 1800 °C. The increase in ε″ is primarily attributed to the rise in electrical conductivity. The conductivity can be determined using equation (6)[54]:

$$\sigma = 2\pi\varepsilon_0\varepsilon\varepsilon'' \quad (6)$$

As present in Figure 8d, the electrical conductivity of GdB_2C_2 powders synthesized at 1500 °C were higher than that of the sample synthesized at 1800 °C. The observed behavior can be predominantly ascribed to the metallic conductivity inherent in the laminated GdB_2C_2 powders. The formation of a finer grain size facilitated the development of a conductive network structure, thereby augmenting the transmission pathways for charge carriers. Through structural optimization, the conductive properties of GdB_2C_2 powder have been significantly enhanced, Thus, it casts a profound influence on the dielectric and the electromagnetic wave absorption traits of the material. This effect primarily arises from the inherent metal conductivity within the layered structure of GdB_2C_2. The diminutive grain size paves the way for the emergence of a seamless conductive network, empowering more expeditious pathways for the conveyance of charge carriers [55]. Furthermore, both the real (ε′) and imaginary (ε″) components of the material's dielectric constant exhibit fluctuations associated with resonance phenomena, providing evidence for nonlinear resonance behavior in GdB_2C_2 that reflects its polarization and relaxation processes. This characteristic is indicative of a favorable dielectric loss performance within the specified frequency range. The material's ability to exhibit such resonant behavior is crucial for its effectiveness in dielectric applications, as it directly impacts the energy storage and dissipation capabilities of the material. Furthermore, the enhanced number of heterogeneous interfaces caused by the smaller grain size also improved relaxation process of GdB_2C_2, which generated the improvement of relaxation polarization.

 doi:10.20944/preprints202405.0725.v1

To evaluate the EMWA capabilities of GdB_2C_2 powder synthesized at elevated temperatures of 1500 °C and 1800 °C, metrics such as reflection loss (RL) and effective absorption bandwidth (EAB) have been employed. Utilizing the calculations prescribed by formulas (7), (8) and (9), we can deduce the RL values, facilitating a quantitative assessment of the material's EMWA performance across varying thermal conditions. This approach enables a nuanced understanding of how temperature influences the electromagnetic properties of GdB_2C_2 powder [56–58]:

$$RL(dB)=20\log|(Z_{in}-Z_0)/(Z_{in}+Z_0)| \quad (7)$$

$$Z_{in}=Z_0\sqrt{\mu_r/\varepsilon_r}\tanh\left[j(2\pi fd/c)\sqrt{\mu_r\varepsilon_r}\right] \quad (8)$$

$$Z_0=\sqrt{\mu_r/\varepsilon_r} \quad (9)$$

Within the equation, Z_0 stands as the emblem of the impedance of free space, with Z_{in} embodying the input impedance. The complex relative permeability, μ_r, unfolds as $\mu'-j\mu''$, and the complex relative permittivity, ε_r, is articulated by $\varepsilon'-j\varepsilon''$. The symbol c embodies the speed of light, d signifies the thickness of the material, and f epitomizes the frequency. Figure 9 dramatically showcases the reflection loss (RL) values for GdB_2C_2 powders forged at 1500 °C and 1800 °C across the expansive frequency realm of 2-18 GHz, with varying thicknesses. The former unveils a minimum reflection loss (RLmin) of -47.01 dB at a frequency of 15.92 GHz, thickness of 3.44 mm, while the latter achieves an RLmin of -29.51 dB, thickness of 4.62 mm, frequency of 16.32 GHz.

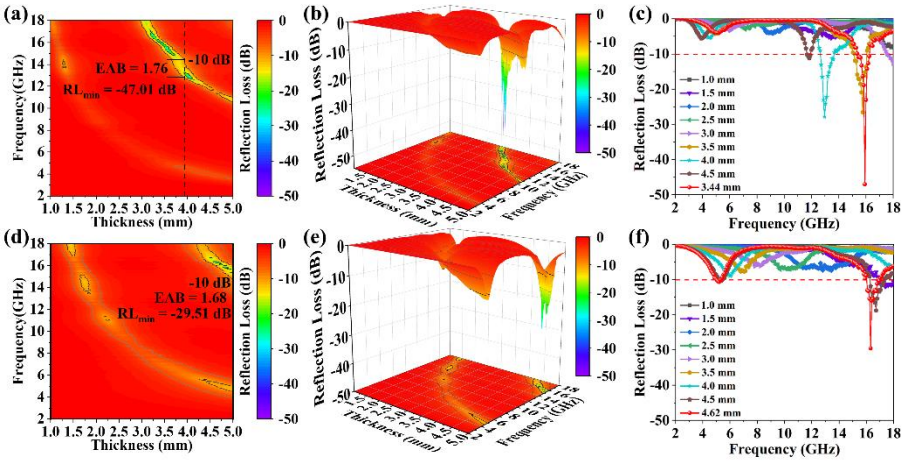

Figure 9. 3D and 2D patterns of Reflection loss values at frequency range of 2 to 18 GHz for different thickness of GdB_2C_2 samples synthesized at 1500 °C (a)(b)(c) and 1800 °C (d) (e)(f).

Theoretically calculated reflection loss (RL) data for different thicknesses of GdB_2C_2 powders synthesized at 1500 °C and 1800 °C in the frequency range of 2-18 GHz are presented in Figures 9c and 9f, respectively, to facilitate a more intuitive comparison of their electromagnetic wave absorption performance. The results clearly demonstrate that the GdB_2C_2 powder synthesized at 1500 °C exhibits a wider electromagnetic absorption bandwidth (EAB), indicating its superior ability to absorb electromagnetic waves. Specifically, for a GdB_2C_2 sample with a thickness of 3.86 mm, the sample synthesized at 1500 °C demonstrates excellent absorption properties by covering a frequency range of approximately 1.76 GHz (Figure 9c). In contrast, even when increasing the thickness of the sample synthesized at 1800 °C to 4.96 mm, its widest EAB can only reach up to 1.68 GHz (Figure 9f), suggesting limited absorption performance. These findings strongly suggest that synthesizing GdB_2C_2 powder at a lower temperature of 1500 °C significantly enhances its electromagnetic wave absorption (EMWA) properties due to finer grain size and improved microstructure optimization leading to enhanced impedance matching and absorption efficiency

The impedance matching (IM, Z) and attenuation capacity of GdB_2C_2 powder synthesized at 1500 °C were investigated to explore the significant enhancement in electromagnetic wave absorption

 doi:10.20944/preprints202405.0725.v1

performance. Figure 10 illustrates the IM (Z) values of these two samples, which are calculated using the following formula to further elucidate the underlying mechanism behind their improved performance[59]:

$$Z = |Z_{in}/Z_0| = \sqrt{\mu_r/\varepsilon_r}\, tanh\left[j(2\pi f d/c)\sqrt{\mu_r \varepsilon_r} \right] \quad (10)$$

IM is a critical factor in determining the EMW entry into material's surface. Optimal IM occurs when the input impedance (Z_{in}) closely matches the air impedance (Z_0). A closer proximity of the impedance matching (IM) value Z to 1 indicates a higher influx of electromagnetic waves into the electromagnetic wave absorber, leading to more efficient impedance characteristic. The frequency range with good impedance matching of the GdB_2C_2 powders synthesized at 1500 °C was larger than that of the sample synthesized at 1800 °C. Consequently, the EMW can effectively penetrate the sample prepared at 1500 °C, the samples synthesized at 1800 °C, however, exhibited significant reflection of electromagnetic wave, attributed to inadequate impedance matching (IM). This discrepancy in EMW interaction with the samples is a direct result of the differing IM values, which influence the absorption efficiency and overall performance of the EMW absorbers.

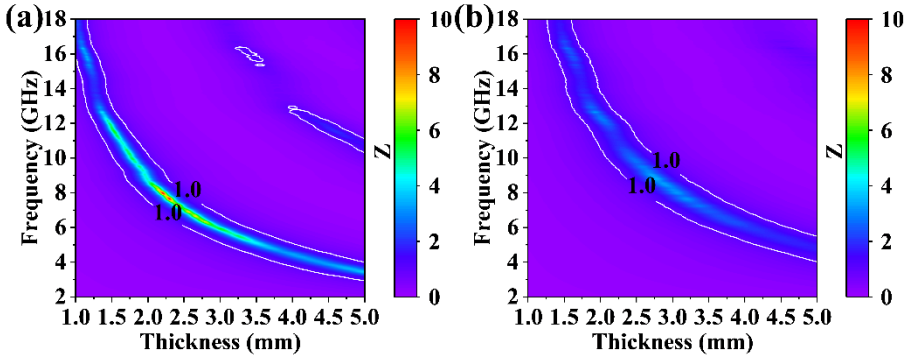

Figure 10. 2D patterns of Z value of GdB_2C_2 samples synthesized at (a) 1500 °C and (b) 1800 °C.

To delve deeper into the electromagnetic energy absorption characteristics of GdB_2C_2 powder across varying temperatures, the attenuation constant (α) was calculated for samples synthesized at 1500 °C and 1800 °C within the wide frequency range of 2 to 18 GHz. This procedure not only elucidates the material's attenuation properties at specific frequencies, moreover, this investigation sheds light on how the preparation temperatures influence the material's capacity to diminish electromagnetic waves. The attenuation constant (α) is ascertainable through the application of the subsequent equation[60]:

$$\alpha = \frac{\sqrt{2}\pi f}{c}\sqrt{(\mu''\varepsilon'' - \mu'\varepsilon') + \sqrt{(\mu''\varepsilon'' - \mu'\mu')^2 + (\mu'\varepsilon'' - \mu''\varepsilon')^2}} \quad (11)$$

The elevation of the α value signifies a heightened capacity of the material to effectively attenuate electromagnetic waves [61]. As depicted in Figure 11, samples prepared at 1500 °C exhibited a higher attenuation constant than those prepared at 1800 °C within the frequency range of 12.64 to 18 GHz. This finding clearly elucidates the impact of different synthesis temperatures on the electromagnetic wave attenuation characteristics of materials. Combined with the calculated IM value, the finer grain size of the sample synthesized at 1500 °C improved the IM as well as the attenuation ability, compared to the sample synthesized at 1800 °C. As a result, the EMWA performance was improved.

 doi:10.20944/preprints202405.0725.v1

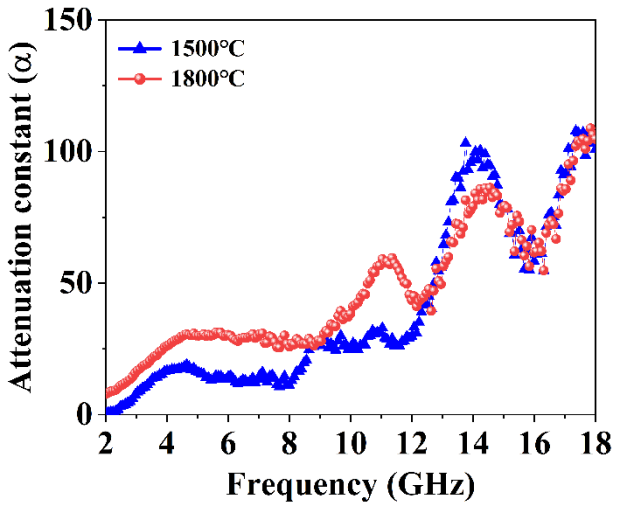

Figure 11. Attenuation constant of GdB_2C_2 samples synthesized at 1500 °C and 1800 °C at the frequency range from 2 to 18 GHz.

Figure 12 shows the absorption mechanism for GdB_2C_2. Initially, the optimal impedance matching (IM) facilitates the penetration of a substantial portion of electromagnetic waves (EMW) into the GdB_2C_2 sample, thereby laying the foundation for its remarkable EMWA capabilities. Following this, the metallic conductivity of GdB_2C_2 plays a pivotal role in inducing conductance loss through electron transition pathways within the material. Furthermore, the presence of a multitude of homogeneous and heterogeneous interfaces in the nano-laminated GdB_2C_2 sample, encompassing GdB_2C_2/GdB_2C_2, GdB_2C_2/paraffin, and GdB_2C_2/GdB_4, significantly amplifies interfacial polarization and electron hopping between GdB_2C_2 nanosheets, thereby elevating dielectric loss. The two-dimensional GdB_2C_2 nanomaterial is transformed into a three-dimensional microscopic framework through its unique layering structure, wherein a network of highly efficient conductive pathways is established. This architectural design not only facilitates the multi-directional scattering and reflection of electromagnetic waves within the material, thereby significantly enhancing its electromagnetic wave absorption capacity, but also results from the coordinated optimization of internal impedance, amplification of conductivity loss, enhanced polarization effect at interfaces and dipoles, as well as combined gain effect arising from their interaction.

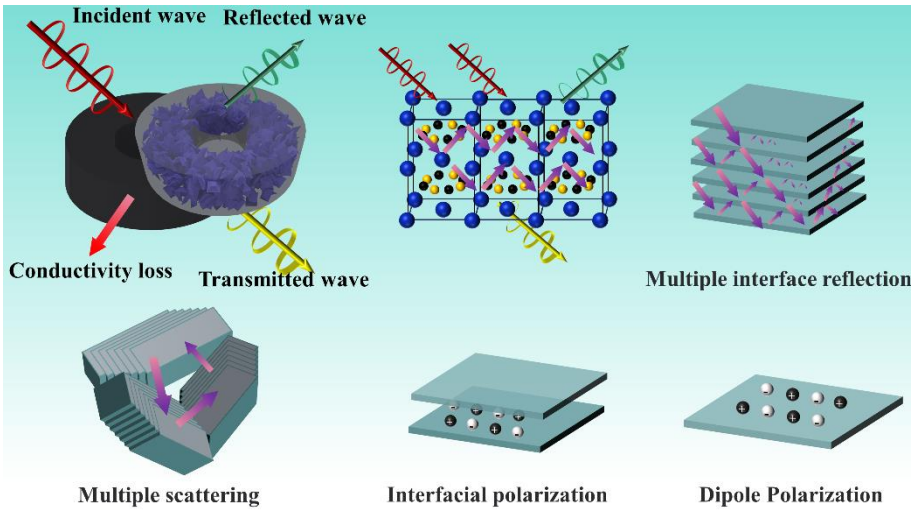

Figure 12. Main EMWA mechanisms of GdB_2C_2.

Figure 13 shows the optimal EMWA performance of ternary layered structure Ti_3SiC_2, Ti_3AlC_2, $Ti_3C_2T_x$, and Ti_3C_2Tx-based materials reported in the relevant literature. Numerous layered structure materials have been thoroughly investigated, and excellent EMWA properties have been achieved in

 doi:10.20944/preprints202405.0725.v1

terms of filler loading, thinner matching thickness, low RL_{min} value and broader EAB. In this study, GdB_2C_2 powders fabricated at 1500 °C presented excellent EMWA properties along with remarkable thermal stability at an ultra-high temperature of 2100 °C.

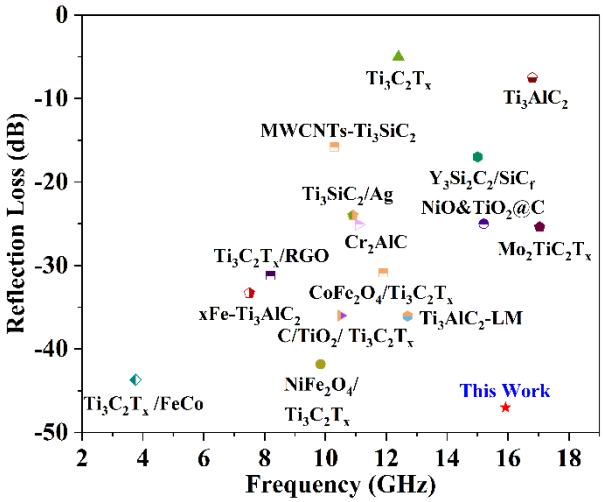

Figure 13. Comparison of electromagnetic wave absorption capacity of GdB_2C_2 with that of other absorbing materials[11,62–74].

4. Conclusions

In summary, we successfully fabricated a novel nanolayered GdB_2C_2 material utilizing in-situ solid phase reaction technology. The formation mechanism of GdB_2C_2 was concluded based on the investigation of the microstructure and phase composition of the samples synthesized at temperatures ranging from 900 °C to 1800 °C. A purity of 96.4 wt. % GdB_2C_2 was obtained at 1500 °C, while a near full pure GdB_2C_2 can be obtained at a temperature over 1700 °C. Noted that the GdB_2C_2 grains were preferred growth along the *c* plane at the temperatures over 1800 °C. In addition, the as-obtained GdB_2C_2 shown excellent thermal stability at high temperature of 2100 °C in Ar atmosphere. This can be ascribed to the high covalent four-members and eight-members B-C rings of GdB_2C_2 which formed a stability frame work. A comparison of EMWA performance on the GdB_2C_2 prepared at 1500 °C and 1800 °C was studied. The GdB_2C_2 material prepared at a temperature of 1500 °C, exhibits the widest EAB of 1.76 GHz and RL_{min} of -47.01 dB (3.44 mm). Such efficacy is the result of its exceptional impedance matching capabilities, efficient conductive dissipation, interfacial polarization, and the multifaceted reflection and scattering across various interfaces. Moreover, the GdB_2C_2 material is anticipated to emerge as a contender for future ultra-high temperature EMWA materials, given the fact that it possesses an excellent thermal stability at ultra-high temperatures.

Acknowledgments: This study was supported by the National Natural Science Foundation of China (Grant No. 12275337, U20B2010 and U2330103), Zhejiang Provincial Natural Science Foundation of China under Grant No. Z24A050005. We would like to recognize the support from the Ningbo Youth Science and Technology Innovation Leading Talent Project (2023QL043).

References

1. Lun, H.; Zeng, Y.; Xiong, X.; Ye, Z.; Zhang, Z.; Li, X.; Chen, H.; Liu, Y. Oxidation behavior of non-stoichiometric (Zr,Hf,Ti)Cx carbide solid solution powders in air. *J. Adv. Ceram.* **2021,** *10*, 741-757.
2. Peters, A. B.; Wang, C.; Zhang, D.; Hernandez, A.; Nagle, D. C.; Mueller, T.; Spicer, J. B. Reactive laser synthesis of ultra-high-temperature ceramics HfC, ZrC, TiC, HfN, ZrN, and TiN for additive manufacturing. *Ceram. Int.* **2023,** *49*, 11204-11229.
3. Yu, Z.; Lv, X.; Lai, S.; Yang, L.; Lei, W.; Luan, X.; Riedel, R. ZrC–ZrB2–SiC ceramic nanocomposites derived from a novel single-source precursor with high ceramic yield. *J. Adv. Ceram.* **2019,** *8*, 112-120.
4. Zhang, Z.; Sha, J.; Zu, Y.; Dai, J.; Liu, Y. Fabrication and mechanical properties of self-toughening ZrB_2–SiC composites from in-situ reaction. *J. Adv. Ceram.* **2019,** *8*, 527-536.

 doi:10.20944/preprints202405.0725.v1

5. Chen, H.; Xiang, H.; Dai, F.-Z.; Liu, J.; Zhou, Y. Low thermal conductivity and high porosity ZrC and HfC ceramics prepared by in-situ reduction reaction/partial sintering method for ultrahigh temperature applications. *J. Mater. Sci. Technol.* **2019,** *35*, 2778-2784.
6. Ren, J.; Zhang, Y.; Zhang, P.; Li, T.; Li, J.; Yang, Y. Ablation resistance of HfC coating reinforced by HfC nanowires in cyclic ablation environment. *J. Eur. Ceram. Soc.* **2017,** *37*, 2759-2768.
7. Ni, D.; Cheng, Y.; Zhang, J.; Liu, J.-X.; Zou, J.; Chen, B.; Wu, H.; Li, H.; Dong, S.; Han, J.; Zhang, X.; Fu, Q.; Zhang, G.-J. Advances in ultra-high temperature ceramics, composites, and coatings. *J. Adv. Ceram.* **2022,** *11*, 1-56.
8. Fu, Y.; Zhang, Y.; Chen, H.; Han, L.; Yin, X.; Fu, Q.; Sun, J. Ultra-high temperature performance of carbon fiber composite reinforced by HfC nanowires: A promising lightweight composites for aerospace engineering. *Compos B Eng.* **2023,** *250*, 110453.
9. Zhang, H.; Tian, X.; Wang, Y.; Ai, S. Study on mechanical properties and thermal conductivity of 3D short carbon fiber reinforced ultra-high temperature ceramic matrix composites: A novel material performance evaluation model. *Comp. Mater. Sci.* **2024,** *237*, 112880.
10. Xia, Y.; Gao, W.; Gao, C. A Review on Graphene-Based Electromagnetic Functional Materials: Electromagnetic Wave Shielding and Absorption. *Adv. Funct. Mater.* **2022,** *32*, 2204591.
11. Zhou, W.; Zhang, Y.; Li, Y.; Gou, Y.; Zhou, X. In-situ synthesis of ternary layered $Y_3Si_2C_2$ ceramic on silicon carbide fiber for enhanced electromagnetic wave absorption. *Ceram Int.* **2022,** *48*, 1908-1915.
12. Li, X.; Li, M.; Lu, X.; Zhu, W.; Xu, H.; Xue, J.; Ye, F.; Liu, Y.; Fan, X.; Cheng, L. A sheath-core shaped ZrO_2-SiC/SiO_2 fiber felt with continuously distributed SiC for broad-band electromagnetic absorption. *Chem Eng J.* **2021,** *419*, 129414.
13. Zhou, W.; Li, Y.; Long, L.; Luo, H.; Wang, Y. High-temperature electromagnetic wave absorption properties of Cf/SiCNFs/Si_3N_4 composites. *J Am Ceram Soc.* **2020,** *103*, 6822-6832.
14. Chen, C.; Xi, J.; Zhou, E.; Peng, L.; Chen, Z.; Gao, C. Porous Graphene Microflowers for High-Performance Microwave Absorption. *Nano-Micro Lett.* **2017,** *10*, 26.
15. Gupta, S.; Tai, N.-H. Carbon materials and their composites for electromagnetic interference shielding effectiveness in X-band. *Carbon.* **2019,** *152*, 159-187.
16. Song, W.; Wang, J.; Fan, L.; Li, Y.; Wang, C.; Cao, M. Interfacial Engineering of Carbon Nanofiber–Graphene–Carbon Nanofiber Heterojunctions in Flexible Lightweight Electromagnetic Shielding Networks. *ACS Appl Mater Interfaces.* **2014,** *6*, 10516-10523.
17. Wang, H.; Zhang, H.; Zhao, K.; Nie, A.; Alharthi, S.; Amin, M. A.; El-Bahy, Z. M.; Li, H.; Chen, L.; Xu, B. B.; Ma, Y.; Li, T. Research progress on electromagnetic wave absorption based on magnetic metal oxides and their composites. *Adv. Compos. Hybrid Mater.* **2023,** *6*, 120.
18. Yang, Q.-x.; Yu, L.-j.; Dong, Y.-b.; Fu, Y.-q.; Zhu, Y.-f. Preparation and microwave absorption properties of magnetic functional porous biomass carbon composites. *Carbon.* **2020,** *158*, 931.
19. Ma, J.; Zhao, B.; Xiang, H.; Dai, F.-Z.; Liu, Y.; Zhang, R.; Zhou, Y. High-entropy spinel ferrites MFe_2O_4 (M = Mg, Mn, Fe, Co, Ni, Cu, Zn) with tunable electromagnetic properties and strong microwave absorption. *J. Adv. Ceram.* **2022,** *11*, 754-768.
20. Zhang, Y.; Gu, J. A Perspective for Developing Polymer-Based Electromagnetic Interference Shielding Composites. *Nano-Micro Lett.* **2022,** *14*, 89.
21. Qin, S.; Cao, Y.; Zhang, J.; Ren, Y.; Sun, C.; Zhang, S.; Zhang, L.; Hu, W.; Yu, M.; Yang, H. Polymer dispersed ionic liquid electrolytes with high ionic conductivity for ultrastable solid-state lithium batteries. *Carbon Energy.* **2023,** *5*, e316.
22. Long, L.; Xu, J.; Luo, H.; Xiao, P.; Zhou, W.; Li, Y. Dielectric response and electromagnetic wave absorption of novel macroporous short carbon fibers/mullite composites. *J Am Ceram Soc.* **2020,** *103*, 6869-6880.
23. De Volder, M. F. L.; Tawfick, S. H.; Baughman, R. H.; Hart, A. J. Carbon Nanotubes: Present and Future Commercial Applications. *Science.* **2013,** *339*, 535-539.
24. Zhu, X.; Qiu, H.; Chen, P.; Chen, G.; Min, W. Graphitic carbon nitride (g-C_3N_4) in situ polymerization to synthesize MOF-Co@CNTs as efficient electromagnetic microwave absorption materials. *Carbon.* **2021,** *176*, 530-539.
25. Liu, F.; Wang, C.; Sui, X.; Riaz, M. A.; Xu, M.; Wei, L.; Chen, Y. Synthesis of graphene materials by electrochemical exfoliation: Recent progress and future potential. *Carbon Energy.* **2019,** *1*, 173-199.
26. Hasani, A.; Teklagne, M. A.; Do, H. H.; Hong, S. H.; Van Le, Q.; Ahn, S. H.; Kim, S. Y. Graphene-based catalysts for electrochemical carbon dioxide reduction. *Carbon Energy.* **2020,** *2*, 158-175.
27. Zhang, Y.; Zhang, Q.; Chen, G. Carbon and carbon composites for thermoelectric applications. *Carbon Energy.* **2020,** *2*, 408-436.
28. Li, M.; Song, X.; Xue, J.; Ye, F.; Yin, L.; Cheng, L.; Fan, X. Construction of Hollow Carbon Nanofibers with Graphene Nanorods as Nano-Antennas for Lower-Frequency Microwave Absorption. *ACS Appl Mater Interfaces.* **2023,** *15*, 31720-31728.

29. Li, M.; Fan, X.; Xu, H.; Ye, F.; Xue, J.; Li, X.; Cheng, L. Controllable synthesis of mesoporous carbon hollow microsphere twined by CNT for enhanced microwave absorption performance. *J. Mater. Sci. Technol.* **2020,** *59*, 164-172.
30. Xiong, X.; Zhang, H.; Lv, H.; Yang, L.; Liang, G.; Zhang, J.; Lai, Y.; Cheng, H.-W.; Che, R. Recent progress in carbon-based materials and loss mechanisms for electromagnetic wave absorption. *Carbon.* **2024,** *219*, 118834.
31. Xia, Q.; Han, Z.; Zhang, Z.; Huang, Z.; Wang, X.; Chang, J.; Chen, Q.; Chen, M. High temperature microwave absorbing materials. *J Mater Chem C.* **2023,** *11*, 4552-4569.
32. Zhou, A.; Liu, Y.; Li, S.; Wang, X.; Ying, G.; Xia, Q.; Zhang, P. From structural ceramics to 2D materials with multi-applications: A review on the development from MAX phases to MXenes. *J. Adv. Ceram.* **2021,** *10*, 1194-1242.
33. Huang, Y.; Lu, Q.; Wu, D.; Jiang, Y.; Liu, Z.; Chen, B.; Zhu, M.; Schmidt, O. G. Flexible MXene films for batteries and beyond. *Carbon Energy.* **2022,** *4*, 598-620.
34. Huang, Z.; Qin, J.; Zhu, Y.; He, K.; Chen, H.; Hoh, H. Y.; Batmunkh, M.; Benedetti, T. M.; Zhang, Q.; Su, C.; Zhang, S.; Zhong, Y. L. Green and scalable electrochemical routes for cost-effective mass production of MXenes for supercapacitor electrodes. *Carbon Energy.* **2023,** *5*, e295.
35. Liu, P.; Liu, W.; Liu, K. Rational modulation of emerging MXene materials for zinc-ion storage. *Carbon Energy.* **2022,** *4*, 60-76.
36. Reckeweg, O.; DiSalvo, F. J. Different Structural Models of YB_2C_2 and GdB_2C_2 on the Basis of Single-Crystal X-Ray Data. *Z.Naturforsch.(B).* **2014,** *69*, 289-293.
37. Xu, H.; Jiang, L.; Chen, K.; Huang, Q.; Zhou, X. High-entropy rare-earth diborodicarbide: A novel class of high-entropy $(Y_{0.25}Yb_{0.25}Dy_{0.25}Er_{0.25})B_2C_2$ ceramics. *J. Adv. Ceram.* **2023,** *12*, 1430-1440.
38. Yamaguchi, Y.; Ohoyama, K.; Yamauchi, H.; Indoh, K.; Onodera, H. Neutron-diffraction study of the magnetic structure of GdB_2C_2. *Appl Phys A.* **2002,** *74*, s877-s879.
39. Roy, L. E.; Hughbanks, T. A Tight-Binding Method for Predicting Magnetic Ordering in Gd-Containing Solids: Application to GdB2C2. *J. Phys. Chem. B.* **2006,** *110*, 20290-20296.
40. Sakai, T.; Adachi, G.-Y.; Shiokawa, J. Electrical properties of rare earth diborodicarbides (RB_2C_2-type layer compounds). *J Less-Common Met.* **1982,** *84*, 107-114.
41. Yang, Y.; Hong, T. Mechanical and thermodynamic properties of YB_2C_2 under pressure. *Physica B.* **2017,** *525*, 154-158.
42. Li, Y.; Tian, L.; Bao, Y.; Chen, J.; Xu, J.; Zhao, G. YB_2C_2: The first damage tolerant ceramic with melting point over 2500 °C. *J Eur Ceram Soc.* **2023,** *43*, 3830-3835.
43. Wu, N.; Zhao, B.; Chen, X.; Hou, C.; Huang, M.; Alhadhrami, A.; Mersal, G. A. M.; Ibrahim, M. M.; Tian, J. Dielectric properties and electromagnetic simulation of molybdenum disulfide and ferric oxide-modified Ti3C2TX MXene hetero-structure for potential microwave absorption. *Adv Compos Hybrid Mater.* **2022,** *5*, 1548-1556.
44. Mudasar, M.; Xu, Z. H.; Lian, S. Y.; Li, X.; Wang, J.; Cheng, X. Featuring heterogeneous composite of W-type hexagonal ferrite with 2D vanadium carbide MXene for wideband microwave absorption. *J. Mater. Res. Technol.* **2024,** *28*, 2699-2713.
45. Jiang, X.; Wang, Q.; Song, L.; Lu, H.; Xu, H.; Shao, G.; Wang, H.; Zhang, R.; Wang, C.; Fan, B. Enhancing electromagnetic wave absorption with core-shell structured SiO2@MXene@MoS2 nanospheres. *Carbon Energy.* **2024**, e502.
46. Li, M.; Zhu, W.; Li, X.; Xu, H.; Fan, X.; Wu, H.; Ye, F.; Xue, J.; Li, X.; Cheng, L.; Zhang, L. $Ti_3C_2T_x/MoS_2$ Self-Rolling Rod-Based Foam Boosts Interfacial Polarization for Electromagnetic Wave Absorption. *Adv Sci.* **2022,** *9*, 2201118.
47. Wang, W.; Yao, D.; Liang, H.; Xia, Y.; Zuo, K.; Yin, J.; Zeng, Y.-P. Improved thermal conductivity of β-Si_3N_4 ceramics through the modification of the liquid phase by using GdH_2 as a sintering additive. *Ceram Int.* **2021,** *47*, 5631-5638.
48. Zeng, X.; Cheng, X.; Yu, R.; Stucky, G. D. Electromagnetic microwave absorption theory and recent achievements in microwave absorbers. *Carbon.* **2020,** *168*, 606-623.
49. Qin, M.; Zhang, L.; Wu, H. Dielectric Loss Mechanism in Electromagnetic Wave Absorbing Materials. *Adv Sci.* **2022,** *9*, 2105553.
50. Du, J.; Li, T.; Xu, Z.; Tang, J.; Qi, Q.; Meng, F. Structure–Activity Relationship in Microstructure Design for Electromagnetic Wave Absorption Applications. *Small Struct.* **2023,** *4*, 2300152.
51. Debye, P. Polar molecules, the chemical catalog company. *Inc., New York.* **1929,** *89*.
52. Li, J.; Xu, T.; Bai, H.; Shen, Z.; Huang, Y.; Xing, W.; Zhou, Z. Structural Modifications and Electromagnetic Property Regulations of Ti_3AlC_2 MAX for Enhancing Microwave Absorption through the Strategy of Fe Doping. *Adv Mater Interfaces.* **2022,** *9*, 2101510.
53. Wu, Z.; Cheng, H.-W.; Jin, C.; Yang, B.; Xu, C.; Pei, K.; Zhang, H.; Yang, Z.; Che, R. Dimensional Design and Core–Shell Engineering of Nanomaterials for Electromagnetic Wave Absorption. *Adv. Mater.* **2022,** *34*, 2107538.

54. Wang, Y.; Zhou, W.; Zeng, G.; Chen, H.; Luo, H.; Fan, X.; Li, Y. Rational design of multi-shell hollow carbon submicrospheres for high-performance microwave absorbers. *Carbon.* **2021,** *175*, 233-242.
55. Tong, Y.; He, M.; Zhou, Y.; Nie, S.; Zhong, X.; Fan, L.; Huang, T.; Liao, Q.; Wang, Y. Three-Dimensional Hierarchical Architecture of the $TiO_2/Ti_3C_2T_x$/RGO Ternary Composite Aerogel for Enhanced Electromagnetic Wave Absorption. *ACS Sustainable Chem Eng.* **2018,** *6*, 8212-8222.
56. Wen, B.; Cao, M.; Hou, Z.; Song, W.; Zhang, L.; Lu, M.; Jin, H.; Fang, X.; Wang, W.; Yuan, J. Temperature dependent microwave attenuation behavior for carbon-nanotube/silica composites. *Carbon.* **2013,** *65*, 124-139.
57. Duan, Y.; Guan, H., *Microwave absorbing materials*. Jenny Stanford Publishing: 2016.
58. Kim, S.; Jo, S.; Gueon, K.; Choi, K.; Kim, J.; Churn, K. Complex permeability and permittivity and microwave absorption of ferrite-rubber composite at X-band frequencies. *IEEE Trans Magn.* **1991,** *27*, 5462-5464.
59. Zhang, W.; Zhang, X.; Zheng, Y.; Guo, C.; Yang, M.; Li, Z.; Wu, H.; Qiu, H.; Yan, H.; Qi, S. Preparation of Polyaniline@MoS_2@Fe_3O_4 Nanowires with a Wide Band and Small Thickness toward Enhancement in Microwave Absorption. *ACS Appl Nano Mater.* **2018,** *1*, 5865-5875.
60. Song, L.; Wu, C.; Zhi, Q.; Zhang, F.; Song, B.; Guan, L.; Chen, Y.; Wang, H.; Zhang, R.; Fan, B. Multifunctional SiC aerogel reinforced with nanofibers and nanowires for high-efficiency electromagnetic wave absorption. *Chem Eng J.* **2023,** *467*, 143518.
61. Qin, G.; Li, Y.; Zhou, W.; Xu, H.; Hu, F.; Zhou, X. In Situ Grown 1D/2D Structure of $Dy_3Si_2C_2$ on SiCw for Enhanced Electromagnetic Wave Absorption. *Materials*. **2023**, *16*, 3455.
62. Feng, W.; Luo, H.; Wang, Y.; Zeng, S.; Tan, Y.; Deng, L.; Zhou, X.; Zhang, H.; Peng, S. Mxenes Derived Laminated and Magnetic Composites with Excellent Microwave Absorbing Performance. *Sci Rep.* **2019,** *9*, 3957.
63. Guo, Y.; Wang, D.; Bai, T.; Liu, H.; Zheng, Y.; Liu, C.; Shen, C. Electrostatic self-assembled $NiFe_2O_4/Ti_3C_2T_x$ MXene nanocomposites for efficient electromagnetic wave absorption at ultralow loading level. *Adv Compos Hybrid Mater.* **2021,** *4*, 602-613.
64. Han, M.; Yin, X.; Li, X.; Anasori, B.; Zhang, L.; Cheng, L.; Gogotsi, Y. Laminated and Two-Dimensional Carbon-Supported Microwave Absorbers Derived from MXenes. *ACS Appl Mater Interfaces.* **2017,** *9*, 20038-20045.
65. Han, M.; Yin, X.; Wu, H.; Hou, Z.; Song, C.; Li, X.; Zhang, L.; Cheng, L. Ti_3C_2 MXenes with Modified Surface for High-Performance Electromagnetic Absorption and Shielding in the X-Band. *ACS Appl Mater Interfaces.* **2016,** *8*, 21011-21019.
66. He, J.; Liu, S.; Deng, L.; Shan, D.; Cao, C.; Luo, H.; Yan, S. Tunable electromagnetic and enhanced microwave absorption properties in $CoFe_2O_4$ decorated Ti_3C_2 MXene composites. *Appl Surf Sci.* **2020,** *504*, 144210.
67. Hu, F.; Wang, X.; Niu, H.; Zhang, S.; Fan, B.; Zhang, R. Synthesis and electromagnetic wave absorption of novel Mo_2TiC_2Tx MXene with diverse etching methods. *J Mater Sci.* **2022,** *57*, 7849-7862.
68. Li, J.; Xu, T.; Bai, H.; Shen, Z.; Huang, Y.; Xing, W.; Zhou, Z. Structural Modifications and Electromagnetic Property Regulations of Ti_3AlC_2 MAX for Enhancing Microwave Absorption through the Strategy of Fe Doping. *Adv. Mater. Interfaces.* **2022,** *9*, 2101510.
69. Li, X.; Wen, C.; Yang, L.; Zhang, R.; Li, X.; Li, Y.; Che, R. MXene/FeCo films with distinct and tunable electromagnetic wave absorption by morphology control and magnetic anisotropy. *Carbon.* **2021,** *175*, 509-518.
70. Tong, Y.; He, M.; Zhou, Y.; Nie, S.; Zhong, X.; Fan, L.; Huang, T.; Liao, Q.; Wang, Y. Three-Dimensional Hierarchical Architecture of the $TiO_2/Ti_3C_2T_x$/RGO Ternary Composite Aerogel for Enhanced Electromagnetic Wave Absorption. *ACS Sustain. Chem. Eng.* **2018,** *6*, 8212-8222.
71. Zhang, Y.; Wen, J.; Zhang, L.; Lu, H.; Guo, Y.; Ma, X.; Zhang, M.; Yin, J.; Dai, L.; Jian, X.; Yin, L.; Xie, J.; Liang, D.; Deng, L. High antioxidant lamellar structure Cr_2AlC: Dielectric and microwave absorption properties in X band. *J Alloy Compd.* **2021,** *860*, 157896.
72. Zhao, K.-Y.; Luo, C.-L.; Sun, C.; Huang, M.-L.; Wang, M. Construction of heterogeneous interfaces on Ti_3AlC_2 micro-particles via surface dotting liquid metal to enhance electromagnetic wave absorption performance. *Compos Pt A-Appl Sci Manuf.* **2023,** *173*, 107640.

 doi:10.20944/preprints202405.0725.v1

73. Liu, Y.; Ji, C.; Su, X.; Xu, J.; He, X. Electromagnetic and microwave absorption properties of Ti_3SiC_2 powders decorated with Ag particles. *J Alloy Compd.* **2020,** *820*, 153154.
74. Zhou, L.; Yu, J.; Wang, H.; Chen, M.; Fang, D.; Wang, Z.; Li, Z. Dielectric and microwave absorption properties of resin-matrix composite coating filled with multi-wall carbon nanotubes and Ti_3SiC_2 particles. *J Mater Sci-Mater Electron.* **2020,** *31*, 15852-15858.